

## Article

# Tensor-based Factorization Algorithms for Pixel-wise Classification of Hyperspectral Data Using Deep Convolutional Networks

Josué López <sup>1,\*</sup>, Deni Torres <sup>1</sup> and Clement Atzberger <sup>3</sup>

<sup>1</sup> Center for Research and Advanced Studies of the National Polytechnic Institute, Telecommunications Group, Av del Bosque 1145, Zapopan 45017, Mexico; dtorres@gdl.cinvestav.mx

<sup>3</sup> University of Natural Resources and Life Science, Institute of Geomatics, Peter Jordan 82, Vienna 1180, Austria; clement.atzberger@boku.ac.at

\* Correspondence: josue.lopez@cinvestav.mx

Version October 30, 2020 submitted to Remote Sens.

**Abstract:** Tensor-based algorithms for data compression have evolved in recent years according to the needs of several research areas. Tucker Decomposition (TKD) is one of the most popular factorization methods based on tensor algebra, but it is clear that it is not the only algorithm which can produce a factorization for a given input data set. Besides, this decomposition does not have singular solutions, i.e., it converges to local minima. Hence, depending on the input data, tensor-based decompositions can achieve better solution to a specific input. The phenomenology of Remote Sensing (RS) Hyperspectral Images (HSI) belongs to the set of natural numbers, i.e., the set of positive integers. Then, a non-negative tensor factorization suggest a more suitable decomposition for positive data by nature. The main purpose of this work is to prove the benefits in processing time, as well as in accuracy, of using a well-posed factorization algorithm. Specifically, this paper performs a quantitative analysis of tensor-based factorization algorithms applied to semantic segmentation of HSI using Deep Convolutional Networks (DCN).

**Keywords:** deep convolutional networks; hyperspectral imagery; tensor decomposition

## 1. Introduction

Big data compression has been one of the most active research areas in recent years [1]. The insertion of tensor-based algorithms for this sort of tasks drove a revolution in several areas such as image processing [2].

Most of the researches in the image processing area require data acquired by multiple sensors. Even in the simplest case, color images, data acquired by three sensors that perceive reflectance of an object are processed. Each sensor receives reflectance in different wavelength ranges, and by merging that data, a color image is produced. Thus, the images can be represented in a form of three-dimensional arrays or third-order tensors. Two dimensions represent the spatial properties and the third dimension denotes the depth, i.e., the spectral bands. Medical analysis [3], mineralogy [4], agriculture [5], radar images [6] and, above all, remote sensing multi- and hyper-spectral images [7] can be represented, by nature, as third-order tensors.

Spectral imagery remarkably aids certain image processing tasks [8]. Recently, the use of this type of data has grown exponentially in various areas such as agriculture [9], medical analysis [10], biomedical [11], natural disaster prediction [12], security affairs [13], among others. The ability to obtain information about a target not only by its reflectance in the spatial domain, but also by response at different wavelengths, has driven a growth in accuracy and precision in tasks such as classification and segmentation [14].

32 Few years ago, several unsupervised classification and segmentation algorithms [] were  
33 developed, taking advantage of the properties that spectral data produce. Subsequently, with the  
34 introduction of supervised machine learning algorithms such as SVM [], kNN [] and ANN [], it was  
35 found that, under certain conditions, there is a direct relationship between the number of bands used  
36 and the performance of these algorithms []. However, with the aim of improving results, neural  
37 network models evolved into deep neural networks []. This caused the computational complexity to  
38 rise considerably and spectral image processing was not easily achievable. The foregoing requires  
39 having robust computer equipment to achieve competitive results in time.

40 Several works opted for matrix factorization algorithm to reduce the high-dimensionality of  
41 spectral images []. More recently, with the development of tensor factorization algorithms [], it has  
42 been found that some algorithms based on tensor algebra produce advantages over those based on  
43 matrices []. Nevertheless, the data produced by both of them are hard to understand for supervised  
44 classification algorithms that need spatial relation between pixels to produce a wise prediction [].

45 In this work, we propose an alternative solution to the problem described previously. To reduce  
46 processing times in supervised classification algorithms, such as deep neural networks, we propose a  
47 model that, from the benefits offered by tensor decomposition algorithms, aids compression of spectral  
48 images. This produces a lower dimensional tensor while preserving the structural and numerical  
49 nature of the original data.

### 50 1.1. State of the art

51 There are several works focused on the development of frameworks that reduce computational  
52 complexity of machine learning algorithms for semantic segmentation of hyperspectral datasets []. The  
53 crucial factor, which is addressed in this work, is to achieve compression of the input data to reduce  
54 the high number of computations, but without sacrificing pixel accuracy, overall accuracy, precision and  
55 recall in the classification task.

56 Before the introduction of tensor decomposition algorithms, the way to use hyperspectral images  
57 as input for supervised classification algorithms was by band selection [23] and [22]. Later, matrix  
58 decomposition algorithms were used, such as PCA in [?], and even non-negative matrix decomposition  
59 methods [?]. In 2015 Zhang et al. [24] were pioneers in experimenting with multilinear algebra-based  
60 decompositions on hyperspectral images.

61 On the other hand, there was also the possibility of using multispectral images due to the small  
62 number of spectral bands, which still made efficient results in classification without dimensionality  
63 reduction achievable, as done in [11], [18], [21] and [?]. However, the need to increase classification  
64 performance forces researchers to use data with more features that favor and aid the classification of  
65 various classes, which are difficult to differentiate with little spectral data. Thus, more recent researches  
66 have decided to use hyperspectral images with tensor decompositions, which has increased the results  
67 in classification accuracy [26], [27], [29], [?] and [?].

68 Recently, Sayeh et al. [?] published a work close to our research. They proposed a non-negative  
69 tensor decomposition of hyperspectral images but, different to our research, they try to preserve certain  
70 spatial-spectral features into the so called abundance maps, i.e. the projection matrices, while this work  
71 pursues to preserve the nature of the image just compressing the main information in the positive core  
72 tensor.

73 Table 1 summarizes some of the most cited related papers, which deal with the  
74 compression-classification issue.

**Table 1.** Related work in spectral imagery semantic segmentation.

Reference	Input	Decomposition	Reduction	Classifier
Li, S. et al. [23] (2014)	HSI	-	Band selection	SVM
Zhang, L. et al. [24] (2015)	HSI	TKD	Spatial-Spectral	-
Wan, Q. et al. [22] (2016)	HSI	-	Band selection	SVM/kNN/CART
Kemker, R. et al. [11] (2017)	MSI	-	-	CNN
Tong L. et al. [] (2017)	HSI	NMF	Unmixing	-
Hamida, A. et al. [21] (2017)	MSI	-	-	CNN
Chien, J. et al. [] (2017)	RGB	TFNN	Spatial-Spectral	TFNN
Dewa, M. et al. [] (2018)	HSI	PCA	Spectral	PCA
Xu, Y. et al. [] (2018)	HSI	-	-	CNN
Li, J. et al. [28] (2019)	MSI	NTD-CNN	Spatial-spectral	-
An, J. et al. [27] (2019)	HSI	T-MLRD	Spatial-spectral	SVM/1NN
An, J. et al. [29] (2019)	HSI	TDA	Spatial-spectral	SVM/1NN
Lopez, J. et al. [] (2019)	MSI	TKD	Spectral	FCN
Sayeh, M. et al. [] (2019)	HSI	NTD	Spatial-Spectral	3D-CNN
<b>Our framework</b>	<b>MSI/HSI</b>	<b>NTKD</b>	<b>Spectral</b>	<b>CNN</b>

### 75 1.2. Contribution

76 In the state of the art we can find a variety of frameworks looking for dimensionality reduction  
 77 of images of any type, that is, RGB [? ], medical [? ], SAR [? ], multispectral [? ], among others.  
 78 In particular, the large number of spectral bands in hyperspectral images has focused efforts in this  
 79 category [? ]. Spatial [? ], spectral [? ] and spatial-spectral [? ] compression have been achieved with  
 80 matrix and tensor decompositions. It is important to highlight that, a decomposition as pre-processing  
 81 for a classification algorithm, instead of favoring, could be counterproductive and greatly affect its  
 82 performance. It is therefore important to make a proper selection of the type of decomposition that  
 83 would produce a suitable data set for post-processing.

84 Unlike previous works, this work seeks to adapt the data in the best way to be the input of deep  
 85 convolutional networks. Convolutional network models are designed to extract and interpret all the  
 86 spatial properties of an image by moving the kernels over the input data []. Therefore, producing  
 87 uncorrelated data in space and spectrum, would make harder the interpretation of the data in the  
 88 convolutional network [? ]. Thus, the proposed framework maintains the positive tensor nature of  
 89 the spectral images and the spatial dimensionality to preserver spatial-spectral correlation of the data  
 90 while reducing the spectral dimensionality, in order to decrease computational load in the pixel-wise  
 91 classification process.

92 We can summarize the contribution of this work with the following two points:

- 93 1. The framework NTKD3-CNN proposed in this work, develops a new strategy to improve  
 94 accuracy results of semantic segmentation convolutional neural networks by finding suitable  
 95 tensor data, preserving spatial correlation and values in the set of the natural numbers while  
 96 compressing the spectral domain and in turn decreasing computational load.
- 97 2. This work also presents an exhaustive performance analysis measuring and comparing its  
 98 efficiency with the most popular metrics, i.e., as pixel accuracy (PA), also PA in function of the  
 99 number of new tensor bands, precision, recall, F1, orthogonality degree of the factor matrices  
 100 and the core tensor, reconstruction error of the original tensor, and execution time.

101 The remainder of this work is organized as follows. Section ?? introduces tensor algebra notation  
 102 and basic concepts to familiarize the reader with the symbology used in this paper. Section ?? presents  
 103 the problem statement of this work and the mathematical definition. In Section 4, CNN theory is  
 104 described for classification and semantic segmentation. Section ?? presents the framework proposed  
 105 for compression and semantic segmentation of spectral images. Experimental results are presented in  
 106 Section ???. Finally, Sections ?? and 8 present a discussion and conclusions based on the results obtained  
 107 in the experiments.

## 108 2. Tensor-Based Factorizations

109 Matrix-based factorizations, such as PCA [] and SVD [] have been significant and useful tools for  
 110 dimensionality reduction and other approaches. Nevertheless, they are limited by representations of  
 111 data in two modes. Most of current applications have data structures often as higher-order arrays, e.g.  
 112 dimensions of space, time, and frequency. This 2-way view in matrix factorizations may be inadequate  
 113 and it is natural to use tensor decomposition approaches [? ].

114 We can define a tensor as a multi-way or multidimensional array. The order of a tensor is the  
 115 number of dimensions, also known as modes, i.e., an  $N$ -order tensor  $\mathbf{X} \in \mathbb{R}^{I_1 \times I_2 \times \dots \times I_N}$  is an  $N$ -dimesional  
 116 array, which elements  $x_{i_1, i_2, \dots, i_N}$  are indexed by  $i_n \in 1, 2, \dots, I_n$  for  $1 \leq n \leq N$ .

117 Throughout this paper, the mathematical notation used by Kolda et al. [17] has been adopted.  
 118 Table 2 summarize this notation.

**Table 2.** Tensor algebra notation summary

$\mathbf{A}, \mathbf{A}, \mathbf{a}, a$	Tensor, matrix, vector and scalar respectively
$\mathbf{A} \in \mathbb{R}^{I_1 \times \dots \times I_N}$	$N$ -order tensor of size $I_1 \times \dots \times I_N$ .
$a_{i_1 \dots i_N}$	An element of a tensor
$\mathbf{a}_{:i_2:i_3}, \mathbf{a}_{i_1::i_3},$ and $\mathbf{a}_{i_1:i_2::}$	Column, row and tube fibers of a third order tensor
$\mathbf{A}_{i_1::}, \mathbf{A}_{:i_2::}, \mathbf{A}_{::i_3::}$	Horizontal, lateral and frontal slices for a third order tensor
$\mathbf{A}^{(n)}, \mathbf{a}^{(n)}$	A matrix/vector element from a sequence of matrices/vectors
$\mathbf{A}_{(n)}$	Mode- $n$ matricization of a tensor. $\mathbf{A}_{(n)} \in \mathbb{R}^{I_n \times \prod_{m \neq n} I_m}$
$\mathbf{X} = \mathbf{a}^{(1)} \circ \dots \circ \mathbf{a}^{(N)}$	Outer product of $N$ vectors, where $x_{i_1 i_2 \dots i_N} = a_{i_1}^{(1)} \dots a_{i_N}^{(N)}$
$\langle \mathbf{A}, \mathbf{B} \rangle$	Inner product of two tensors.
$\mathbf{B} = \mathbf{A} \times_n \mathbf{U}$	$n$ -mode product of tensor $\mathbf{A} \in \mathbb{R}^{I_1 \times \dots \times I_N}$ by a matrix $\mathbf{U} \in \mathbb{R}^{J \times I_n}$ along axis $n$ .

### 119 2.1. Basic concepts

120 It is also necessary to introduce some tensor algebra operations and basic concepts used in later  
 121 explanations. These notations were taken textually from [17].

#### 122 2.1.1. Matricization

123 The mode- $n$  matricization is the process of reordering the elements of a tensor into a matrix along  
 124 axis  $n$  and it is denoted as  $\mathbf{A}_{(n)} \in \mathbb{R}^{I_n \times \prod_{m \neq n} I_m}$ .

#### 125 2.1.2. Outer Product

126 The outer product of  $N$  vectors  $\mathbf{X} = \mathbf{a}^{(1)} \circ \dots \circ \mathbf{a}^{(N)}$  produces a tensor  $\mathbf{X} \in \mathbb{R}^{I_1 \times \dots \times I_N}$   
 127 where  $\circ$  denotes the outer product and  $\mathbf{a}^{(n)}$  denotes a vector in a sequence of  $N$  vectors  
 128 and each element of the tensor is the product of the corresponding vector elements; i.e.,  
 129  $x_{i_1 i_2 \dots i_N} = a_{i_1}^{(1)} \dots a_{i_N}^{(N)}$ .

#### 130 2.1.3. Inner Product

131 The inner product of two tensors  $\mathbf{A}, \mathbf{B} \in \mathbb{R}^{I_1 \times \dots \times I_N}$  is the sum of the products of their entries;  
 132 i.e.,  $\langle \mathbf{A}, \mathbf{B} \rangle = \sum_{i_1=1}^{I_1} \dots \sum_{i_N=1}^{I_N} a_{i_1 \dots i_N} b_{i_1 \dots i_N}$ .

#### 133 2.1.4. $N$ -Mode Product

134 It means the multiplication of a tensor  $\mathbf{A} \in \mathbb{R}^{I_1 \times \dots \times I_N}$  by a matrix  $\mathbf{U} \in \mathbb{R}^{J \times I_n}$  or vector  $\mathbf{u} \in \mathbb{R}^{I_n}$  in  
 135 mode  $n$ ; i.e., along axis  $n$ . It is represented by  $\mathbf{B} = \mathbf{A} \times_n \mathbf{U}$ , where  $\mathbf{B} \in \mathbb{R}^{I_1 \times \dots \times I_{n-1} \times J \times I_{n+1} \times \dots \times I_N}$  [17].

#### 136 2.1.5. Rank-One Tensor

137 A tensor  $\mathbf{X} \in \mathbb{R}^{I_1 \times \dots \times I_N}$  is rank one if it can be written as the outer product of  $N$  vectors;  
 138 i.e.,  $\mathbf{X} = \mathbf{a}^{(1)} \circ \dots \circ \mathbf{a}^{(N)}$ .

<sup>139</sup> 2.1.6. Rank-R Tensor

<sup>140</sup> The rank of a tensor  $\mathfrak{X}$  is the smallest number of components in a CPD; i.e., the smallest  
<sup>141</sup> number of rank-one tensors that generate  $\mathfrak{X}$  as their sum [17].

<sup>142</sup> 2.1.7. N-Rank

<sup>143</sup> The  $n$ -rank of a tensor  $\mathfrak{X} \in \mathbb{R}^{I_1 \times \dots \times I_N}$  denoted  $\text{rank}_n(\mathfrak{X})$ , is the column rank of  $\mathbf{X}_{(n)}$ ; i.e., the  
<sup>144</sup> dimension of the vector space spanned by the mode- $n$  fibers. Hence, if  $R_n \equiv \text{rank}_n(\mathfrak{X})$  for  $n = 1, \dots, N$ ,  
<sup>145</sup> we can say that  $\mathfrak{X}$  has a rank –  $(R_1, \dots, R_N)$  tensor.

<sup>146</sup> 2.2. Nonnegative Tucker Decomposition (NTKD)

<sup>147</sup> The TKD, also called the Tucker3 for the particular case of third-order tensors, or best rank  $(J_1,$   
<sup>148</sup>  $J_2, J_3)$  approximation, can be formally formulated as follows [? ]. Given a third-order data tensor  
<sup>149</sup>  $\mathfrak{X} \in \mathbb{R}^{I_1 \times I_2 \times I_3}$  and three positive indices  $J_1, J_2$  and  $J_3$ , find a core tensor  $\mathfrak{G} \in \mathbb{R}^{J_1 \times J_2 \times J_3}$  and three  
<sup>150</sup> component matrices called factor or loading matrices  $\mathbf{U}_1 \in \mathbb{R}^{I_1 \times J_1}$ ,  $\mathbf{U}_2 \in \mathbb{R}^{I_2 \times J_2}$  and  $\mathbf{U}_3 \in \mathbb{R}^{I_3 \times J_3}$  which  
<sup>151</sup> perform the following approximate decomposition:

$$\mathfrak{X} = \mathfrak{G} \times_1 \mathbf{U}^{(1)} \dots \times_N \mathbf{U}^{(N)} + \mathcal{E} \quad (1)$$

<sup>152</sup> where  $\mathcal{E}$  denotes the approximation error. The core tensor  $\mathfrak{G}$  preserves the level of interaction for each  
<sup>153</sup> factor or projection matrix  $\mathbf{U}^{(n)}$ . The factor matrices are commonly considered orthogonal, but in  
<sup>154</sup> Tucker models with non-negativity constraints, that is not necessarily imposed [? ]. These matrices  
<sup>155</sup> can be seen as the principal components in each mode [17] (see Figure 1).  $J_n$  represents the number of  
<sup>156</sup> components in the decomposition; i.e., the rank –  $(R_1, \dots, R_N)$ .

<sup>157</sup> We can also denote the TKD using the matricization approach and express it by

$$\mathbf{X}_{(1)} = \mathbf{U}^{(1)} \mathbf{G}_{(1)} (\mathbf{U}^{(3)} \otimes \mathbf{U}^{(2)})^T \quad (2a)$$

$$\mathbf{X}_{(2)} = \mathbf{U}^{(2)} \mathbf{G}_{(2)} (\mathbf{U}^{(3)} \otimes \mathbf{U}^{(1)})^T \quad (2b)$$

$$\mathbf{X}_{(3)} = \mathbf{U}^{(3)} \mathbf{G}_{(3)} (\mathbf{U}^{(2)} \otimes \mathbf{U}^{(1)})^T \quad (2c)$$

<sup>158</sup> where  $\otimes$  denotes the Kronecker product and  $\mathbf{X}_{(n)}$  and  $\mathbf{G}_{(n)}$  are the  $n$ -mode matricized versions of  
<sup>159</sup> tensor  $\mathfrak{X}$  and  $\mathfrak{G}$  respectively.

<sup>160</sup> Starting from (1), the reconstruction of an approximated tensor can be given by

$$\hat{\mathfrak{X}} = \mathfrak{G} \times_1 \mathbf{U}^{(1)} \dots \times_N \mathbf{U}^{(N)} \quad (3)$$

<sup>161</sup> where  $\hat{\mathfrak{X}}$  is the reconstructed tensor.

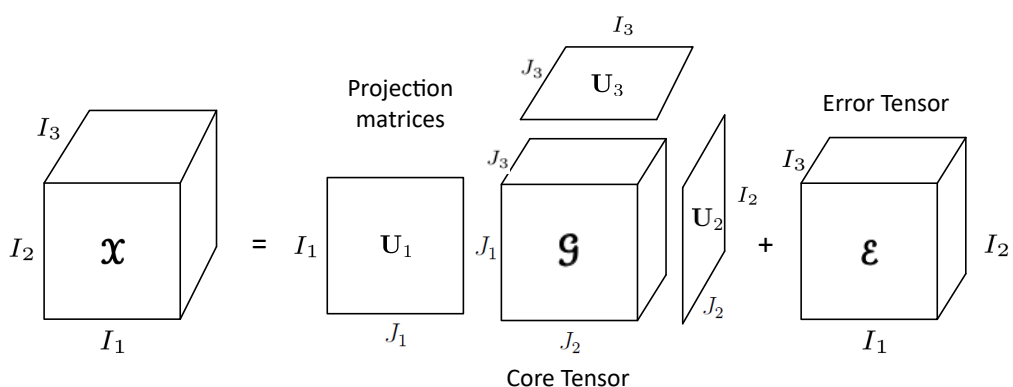


**Figure 1.** Tucker decomposition for a third-order tensor.

162 Then, we can acquire the core tensor  $\mathbf{G}$  by the multilinear projection

$$\mathbf{G} = \mathbf{X} \times_1 \mathbf{U}^{(1)\top} \cdots \times_N \mathbf{U}^{(N)\top} \quad (4)$$

163 where  $\mathbf{U}^{(n)\top}$  denotes the transpose matrix of  $\mathbf{U}^{(n)}$  for  
 164  $n = 1, \dots, N$ . The reconstruction error  $\xi$  can be computed as

$$\xi(\hat{\mathbf{X}}) = \|\mathbf{X} - \hat{\mathbf{X}}\|_F^2 \quad (5)$$

165 where  $\|\cdot\|_F$  represents the Frobenius norm. To compute the best rank approximation of a tensor, it is  
 166 required an iterative algorithm. HOSVD, ALS and HOOI are algorithms commonly used in TKD [? ].

167 HOOI initializes the factors matrices using HOSVD and assumes that orthogonal matrices are  
 168 known, so that the core tensor is obtained with (4). Then, it maximizes the cost function

$$\max_{\mathbf{U}^{(1)}, \mathbf{U}^{(2)}, \mathbf{U}^{(3)}} \|\mathbf{X} \times_1 \mathbf{U}^{(1)\top} \times_2 \mathbf{U}^{(2)\top} \cdots \times_N \mathbf{U}^{(N)\top}\|_F^2 \quad (6)$$

169 with  $\mathbf{U}^{(n)}$  unknown. Fixing all factor matrices but one, tensor  $\mathbf{X}$  can be projected onto the  
 170  $\{R_1, \dots, R_{n-1}, R_{n+1}, \dots, R_N\}$ -dimensional space as

$$\mathbf{W}^{(-n)} = \mathbf{X} \times_1 \mathbf{U}^{(1)\top} \cdots \times_{n-1} \mathbf{U}^{(n-1)\top} \times_{n+1} \mathbf{U}^{(n+1)\top} \cdots \times_N \mathbf{U}^{(N)\top} \quad (7)$$

171 and the orthogonal matrices can be estimated as an orthonormal basis for the dominant subspace  
 172 of the projection by applying the standard matrix SVD for mode- $n$  unfolded matrix  $\mathbf{W}_{(n)}^{(-n)}$  [? ]. See  
 173 Algorithm 1.

174 The HOOI algorithm evidently can be applied for the particular case of third-order tensor.  
 175 Furthermore, it can be slightly adjusted for preserving any input dimension and develop the  
 176 decomposition in a specific order. This will be explained in next chapters.

---

**Algorithm 1:** HOOI algorithm to compute a rank- $(R_1, \dots, R_N)$  TKD for an  $N$ th-order tensor  
 $\mathbf{X} \in \mathbb{R}^{I_1 \times \dots \times I_N}$ .

---

**Function** HOOI( $\mathbf{X}, J_1, \dots, J_N$ ):

  initialize  $\mathbf{U}^{(n)} \in \mathbb{R}^{I_n \times J_n}$  for  $n = 1, \dots, N$  using HOSVD or random

**repeat**

**for**  $n = 1, \dots, N$  **do**

$\mathbf{W}^{(-n)} \leftarrow \mathbf{X} \times_{-n} \{\mathbf{U}^\top\}$

$[\mathbf{U}^{(n)}, \Sigma^{(n)}, \mathbf{V}^{(n)}] \leftarrow \text{svds}(\mathbf{W}_{(n)}^{(-n)}, J_n, 'LM')$

$\mathbf{U}^{(n)} \leftarrow [\mathbf{U}^{(n)}]_+$

**end**

**until** fit ceases to improve or maximum iterations exhausted;

$\mathbf{G} \leftarrow \mathbf{W}^{(-N)} \times_N \mathbf{U}^{(N)\top}$

**Output:**  $\mathbf{U}^{(n)} \in \mathbb{R}_+^{I_n \times J_n}$ ,  $\mathbf{G} \in \mathbb{R}_+^{J_1 \times J_2 \times \dots \times J_N}$

---

### 179 3. Problem phenomenology

#### 180 3.1. Spectral Imagery

181 Multi- or Hyper-spectral images are by nature multidimensional nonnegative arrays. A spectral  
 182 image can be sorted and represented as a third-order tensor  $\mathbf{X} \in \mathbb{R}_+^{I_1 \times I_2 \times I_3}$ , where  $I_1, I_2$  and  $I_3$  represent  
 183 its height, width and spectral bands respectively. In RS image processing, spectral images are frequently  
 184 used for classification of different material in a scene of interest. However, due to the low spatial

185 resolution produced by the distance between the sensor and the target, spatial features are not sufficient  
186 to discern certain classes. That is why spectral resolution plays an important role in this type of task.

187 The separation into spectral bands allows perception of reflectance at different wavelengths. This  
188 helps to better characterize various materials, in order to simplify the process of discernment between  
189 classes. The effort to obtain these spectral features generates a greater amount of data, which increases  
190 the processing complexity. This is where the spectral decomposition task becomes relevant.

### 191 3.2. Problem Statement

192 Given a Spectral Image as a third-order tensor  $\mathbf{X} \in \mathbb{R}^{I_1 \times I_2 \times I_3}$ , and its corresponding pixelwise  
193 classification ground truth matrix  $\mathbf{Y} \in \mathbb{R}^{I_1 \times I_2}$  for a specific number of classes  $C$ , find, through  
194 Non-negative Tensor Decomposition, the best rank- $(R_1, R_2, R_n)$  approximation and its respective  
195 core tensor  $\mathbf{G} \in \mathbb{R}^{I_1 \times I_2 \times I_3}$ , where  $R_1 = I_1, R_2 = I_2$  and  $R_3 = J_3 << I_3$ , to be the input of a pixel-wise  
196 classification Convolutional Neural Network and produce an output matrix  $\hat{\mathbf{Y}}$  of predicted classes,  
197 achieving competitive performance metrics for pixel-wise classification while decreasing computational  
198 load in the classification process.

### 199 3.3. Mathematical Definition

200 We can mathematically define the problem statement described above as an optimization problem.

$$\begin{aligned} & \min_{\mathbf{G}, \mathbf{U}^{(1)}, \mathbf{U}^{(2)}, \mathbf{U}^{(3)}} \|\mathbf{X} - \mathbf{G} \times_1 \mathbf{U}^{(1)} \times_2 \mathbf{U}^{(2)} \times_3 \mathbf{U}^{(3)}\|_F^2 \\ & \text{subject to } \mathbf{U}^{(n)} \in \mathbb{R}_+^{I_n \times J_n} \quad \text{for } n = 1, 2, 3 \quad \text{and } \mathbf{G} \in \mathbb{R}_+^{I_1 \times I_2 \times J_3} \\ & \quad J_1 = I_1, J_2 = I_2 \quad \text{no compression in the spatial domain,} \\ & \quad J_3 << I_3 \quad \text{reduced spectral domain at the core tensor,} \\ & \quad \xi(\hat{\mathbf{X}}) \rightarrow 0 \quad \text{and } PA \geq \psi \quad \text{competitive pixel accuracy up to a threshold} \end{aligned} \tag{8}$$

## 201 4. Deep Convolutional Neural Networks (DCNNs)

CNNs are supervised feed-forward DL-ANNs for computer vision. The idea of applying a sort of convolution of the synaptic weights of a neural network through the input data yields to a preservation of spatial features, which alleviates the hard task of classification and in turn semantic segmentation. This type of ANN works under the same linear regression model as every machine learning (ML) algorithm. Since images are three dimensional arrays, we can use tensor algebra notation to describe the input of CNNs as a tensor  $\mathbf{A} \in \mathbb{R}^{I_1 \times I_2 \times I_3}$ , where  $I_1, I_2$ , and  $I_3$  represent height, width, and depth of the third order array respectively; i.e., the spatial and spectral domain of an image. We can write generally the linear regression model used for ANNs as

$$\hat{\mathbf{y}} = \sigma(\mathbf{W}\mathbf{g} + \mathbf{b}) \tag{9}$$

where  $\hat{\mathbf{y}}$  represents the output prediction of the network;  $\sigma$  denotes an activation function;  $\mathbf{g}$  is the input dataset;  $\mathbf{W}$  and  $\mathbf{b}$  are the matrix of synaptic weights and the bias vector, respectively. These parameters are adjustable; i.e., their values are modified every iteration looking for convergence to minimize the loss in the prediction through optimization algorithms [32]. For simplicity, the bias vector can be ignored, assuming that matrix  $\mathbf{W}$  will update until convergence independently of another parameter [32]. Considering that the input dataset to a CNN is a multidimensional array, we can represent (??) and (9) using tensor algebra notation as

$$\hat{\mathbf{y}} = \sigma(\mathbf{W}\mathbf{G}) \tag{10}$$

where  $\hat{\mathbf{y}}$  represents the prediction output tensor of the ANN (in our case, a second order tensor or matrix  $\hat{\mathbf{Y}}$ ),  $\mathbf{G}$  is the input dataset, and  $\mathbf{W}$  is a  $K_1 \times K_2 \times F_1$  tensor called filter or kernel with the adaptable synaptic weights. Different to conventional ANN, in CNNs,  $\mathbf{W}$  is a shiftable square tensor is much smaller in height and width than the input data, i.e.,  $K_1 = K_2$  and  $K_s \ll I_s$  for  $s = 1, 2$ ;  $F_1$  denotes the number of input channels; i.e.,  $F_1 = I_3$ . For hidden layers, instead of the prediction tensor  $\hat{\mathbf{y}}$ , the output is a matrix called activation map  $\mathbf{M} \in \mathbb{R}^{I_1 \times I_2}$ , which preserves features from the original data in each domain. Actually, it is necessary to use much kernels  $\mathbf{W}^{(f_2)}$  as activation maps, with different initialization values to preserve diverse features of the image. Hence, we can also define activation maps as a tensor  $\mathcal{M} \in \mathbb{R}^{I_1 \times I_2 \times F_2}$  where  $F_2$  denotes the number of activation maps produced by each filter (see Figure 2). Kernels are displaced through the whole input image as a discrete convolution operation. Then, each element of the output activation map  $m_{i_1 i_2 f_2}$  is computed by the summary of the Hadamard product of kernel  $\mathbf{W}^{(f_2)}$  and a subtensor from the input tensor  $\mathbf{G}$  centered in position  $(i, j)$  and with same dimensions of  $\mathbf{W}$ , as follows

$$m_{i_1 i_2 f_2} = \sigma \left[ \sum_{k_1=1}^{K_1} \sum_{k_2=1}^{K_2} \sum_{f_1=1}^{F_1} w_{k_1, k_2, f_1} g_{i_1+k_1-o_1, i_2+k_2-o_2, f_1} \right] \quad (11)$$

where  $m_{i_1 i_2 f_2}$  denotes the value of the output activation map  $f_2$  at position  $i_1, i_2$ ;  $\sigma$  represents the activation function; and  $o_1$  and  $o_2$  are offsets in spatial dimensions which depend on the kernel size, and equal  $\frac{K_1+1}{2}$  and  $\frac{K_2+1}{2}$  respectively (see Figure 2).

205

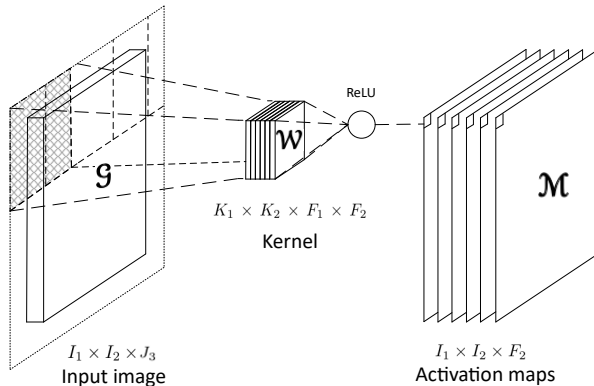


**Figure 2.** Convolutional layer with a  $K_1 \times K_2 \times F_1 \times F_2$  kernel. Input channels  $F_1$  must equal the spectral bands  $I_3$ . To preserve original dimensions at the output, zero padding is needed [18]. Output dimensions also depend on stride  $S = 1$  to consider every piece of pixel information and to preserve original dimensions.

An ANN is trained by using iterative gradient-based optimizers, such as Stochastic gradient descent, Momentum, RMSprop, and Adam [32]. This drive the cost function  $L(\mathbf{W})$  to a very low value by updating the synaptic weights  $\mathbf{W}$ . We can compute the cost function by any function that measures the difference between the training data and the prediction, such as Euclidean distance or cross-entropy [10]. Besides, the same function is used to measure the performance of the model during testing and validation. In order to avoid overfitting [32], the total cost function used to train an ANN combines one of the cost functions mentioned before, plus a regularization term.

$$J(\mathbf{W}) = L(\mathbf{W}) + R(\mathbf{W}), \quad (12)$$

where  $J(\mathbf{W})$  denotes the total cost function and  $R(\mathbf{W})$  represents a regularization function. Then, we can decrease  $J(\mathbf{W})$  by updating the synaptic weights in the direction of the negative gradient. This is known as the method of steepest descent or gradient descent.

$$\mathbf{W}' = \mathbf{W} - \alpha \nabla_{\mathbf{W}} J(\mathbf{W}), \quad (13)$$

where  $\mathbf{W}'$  represents the synaptic weights tensor in next iteration during training,  $\alpha$  denotes the learning rate parameter, and  $\nabla_{\mathbf{W}} J(\mathbf{W})$  the cost function gradient. Gradient descent converges when every element of the gradient is zero, or in practice, very close to zero [10].

CNNs has been successfully used in many image classification frameworks. This variation in architecture from other typical ANN models yields the network to learn spatial and spectral features, which are highly profitable for image classification. Besides, FCNs, constructed with only convolutional layers are able to classify each element of the input image; i.e., they yield pixel-wise classification, or in other words, semantic segmentation.

## 5. NTD for DCNNs

Consider an input dataset  $\mathbf{X} \in \mathbb{N}^{I_1 \times I_2 \times I_3}$  with  $I_1 \times I_2 \times I_3$  samples, where the in the space of the natural numbers  $\mathbb{N}$ , where a fiber  $\mathbf{x}_{i_1 i_2}$  represents the endmember of pixel  $i_1, i_2$  and can be represented by the Linear Mixing Model (LMM) as follows

$$\mathbf{x}_{i_1 i_2} = \sum_{c=1}^C (\alpha_{i_1 i_2 c} \mathbf{m}_c + \boldsymbol{\eta}) \quad (14)$$

where  $\alpha_c$  is the contribution of material  $c$  at pixel  $i_1 i_2$ ,  $\mathbf{m}_c$  denotes the spectral signature of a specific material  $c$ , and  $\boldsymbol{\eta}$  represents an additive noise vector. Figure 3 shows the spectral signatures for the Indian Pines dataset.

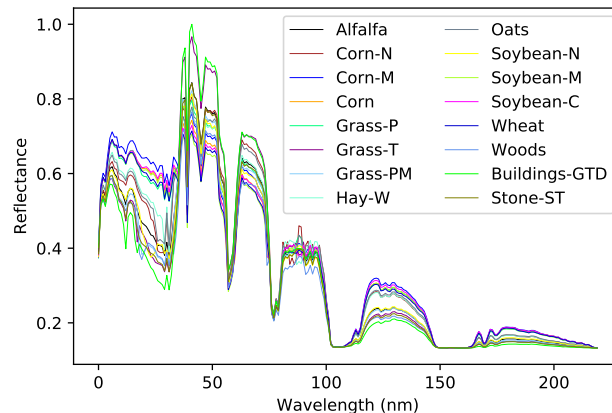


**Figure 3.** Spectral signatures of 16 materials from the Indian Pines dataset.

Let  $\mathbf{Y} \in \mathbb{C}^{I_1 \times I_2}$  be the matrix of actual classes corresponding our dataset  $\mathbf{X}$  and  $\mathbb{C}$  defines the set of  $C$  different classes. Besides, let  $\hat{\mathbf{Y}} \in \mathbb{C}^{I_1 \times I_2}$  be the matrix of a predicted class prediction produced by a classifier  $\Theta$ , where  $y_{i_1 i_2}$  and  $\hat{y}_{i_1 i_2}$  are the actual class and the predicted class of pixel  $i_1, i_2$  respectively.

In order to reduce data dimensionality of the input dataset  $\mathbf{X}$ , we use the restricted NTD  $\mathcal{T}$ , producing a core tensor  $\mathbf{G} \in \mathbb{N}^{I_1 \times I_2 \times J_3}$  and  $n$  factors matrices  $\mathbf{U}^{(n)}$  i.e.,  $\mathbf{X} \xrightarrow{\mathcal{T}} (\mathbf{G}, \mathbf{U}^{(n)})$ , where the core tensor is restricted to preserve the spatial dimensions and to be in the set of the natural numbers. Hence, each fiber of the core tensor, i.e.,  $\mathbf{x}_{i_1 i_2}$  takes a new representation in a space called tensor bands the tensor bands space. Figure 4 shows the spectral signatures for the Indian Pines dataset.

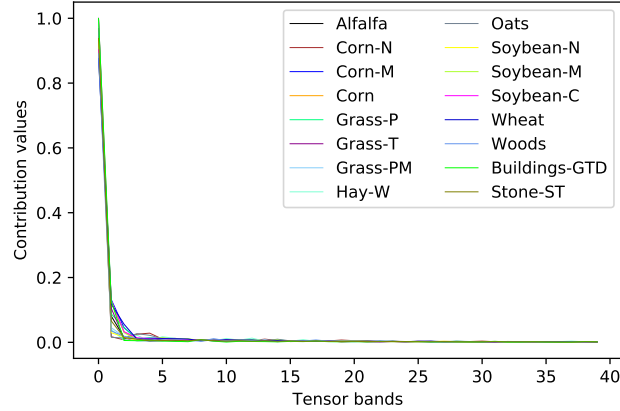


**Figure 4.** Tensor bands signatures of 16 materials from the Indian Pines dataset.

229 In this paper, we aim to feed supervised classifiers based on DCNN, with a lower dimensional  
 230 tensor than the original dataset. This has three particular motivations: 1) to avoid overfitting the  
 231 DCNN, 2) to reduce the computational complexity, and 3) keep the classifier performance while  
 232 reducing the execution time. We can see in Figure 4 the new tensor bands values for each class,  
 233 or, in other words, the singular values at the core tensor generated by the NTD. The first tensor  
 234 bands provide information to differentiate the classes of interest from the input dataset. Therefore,  
 235 the core tensor  $\mathbf{g} \in \mathbb{N}^{I_1 \times I_2 \times I_3}$ , with  $I_3 < J_3$ , and its corresponding ground truth  $\mathbf{Y}$  are the input tuple  
 236 for the DCNN classifier  $\Theta$ , which produce the predicted label for each element of the input, i.e.,

$$(\mathbf{g}, \mathbf{Y}) \xrightarrow{\Theta} \hat{\mathbf{Y}} \quad (15)$$

237 We show the big picture of the framework proposed in this work in Figure 5.

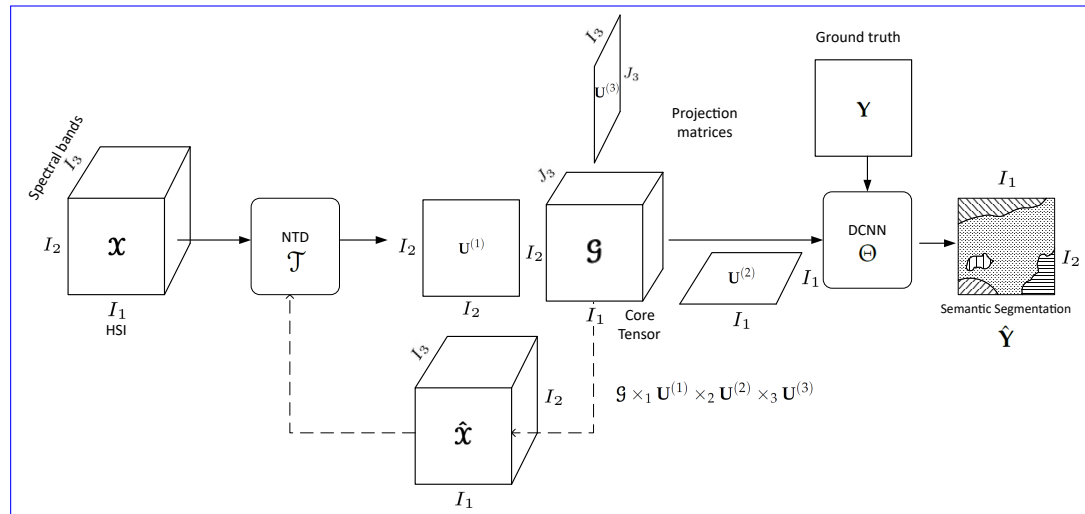


**Figure 5.** Big picture of the framework proposed.

238 The performance of our classification model can be measured by the cross-entropy loss, whose  
 239 output is a probability value. The cross-entropy loss increases as the predicted probability diverges  
 240 from the actual label and it is computed as

$$J(\mathbf{W}) = -\mathbb{E}_{\mathbf{g}, \mathbf{Y} \sim p} \log p(\mathbf{Y} | \mathbf{g}) \quad (16)$$

241 where  $J(\mathbf{g})$  represents the loss function. For a multiclass probability distribution, the cross entropy  
 242 cost function can be written as

$$H(y, p) = - \sum_{c=1}^C y_c \log(p_c) \quad (17)$$

243 where  $H(y, p)$  denotes the cross entropy of targets  $y$  with a probability  $p$ .

244 Any time we wish to represent a probability distribution over a discrete variable with  $C$  possible  
 245 values, we may use the softmax function. Thus, we use the softmax function as the output of our  
 246 classifier, to represent the probability distribution over  $C$  different classes. Formally, the softmax  
 247 function is given by

$$\text{softmax}(z)_l = \frac{e^{z_l}}{\sum_{m=1}^M e^{z_m}} \quad (18)$$

## 248 6. Experimental Results

### 249 6.1. Input Data

250 For this work, we chose three of the most popular multi- and hyperspectral dataset for  
 251 classification.

#### 252 6.1.1. Sentinel-2 CNNMSI

253 This dataset developed by Lopez et al. [?] is composed of RS Sentinel-2 scenarios from central  
 254 Europe. It has 100 scenarios for the training space and 10 scenarios for testing, all of them with  
 255  $128 \times 128$  pixels with spatial resolution of  $20m^2$  and 9 spectral bands in the range  $490 - 2190nm$ .  
 256 The labels are semi-manually assigned for five classes of interest: vegetation, soil, water, clouds and  
 257 shadows. Data are available in the link [Sentinel-2 Dataset](#).

Table 3. Average of contribution per class in Sentinel-2 dataset.

Class	Dataset (%)	Train (%)	Test (%)
Soil	23.58	22.87	30.73
Shadow	2.52	2.58	1.91
Cloud	13.87	14.37	8.83
Water	12.13	11.93	14.10
Vegetation	47.88	48.23	44.41

#### 258 6.1.2. Indian Pines

259 This dataset is a scene produced by AVIRIS in North-western Indiana and consists of  $145 \times 145$   
 260 pixels and 224 spectral bands in the wavelength range  $0.4 - 2.5\mu m$ . The Indian Pines scene contains  
 261 two-thirds agriculture, and one-third forest or other natural perennial vegetation. There are two major  
 262 dual lane highways, a rail line, as well as some low density housing, other built structures, and smaller  
 263 roads. Since the scene is taken in June some of the crops present, corn, soybeans, are in early stages of  
 264 growth with less than 5% coverage. The ground truth available is designated into sixteen classes and  
 265 is not all mutually exclusive. Indian Pines data are available at [Indian Pines dataset](#).

#### 266 6.1.3. Salinas

267 This scene was collected by the AVIRIS sensor over Salinas Valley, California. It has  $512 \times 217$   
 268 pixels with spatial resolution  $3.7m$ , and 224 spectral bands. It includes vegetables, bare soils, and  
 269 vineyard fields. Salinas groundtruth contains 16 classes.

**Table 4.** Summary of the different dataset used for experiments in this work.

Dataset	Spatial dimensions	Bands	Classes	Samples
Sentinel-2 CNNMSI	$128 \times 128$	5	9	147,456
Indian Pines	$145 \times 145$	224	16	4,709,600
Salinas	$512 \times 217$	224	16	24,887,296

270 6.2. Metrics

271 6.2.1. Relative Mean Square Error (rMSE)

272 In order to compute the reconstruction error of the tensor  $\mathbf{X}$  for the implementation of HOOI,  
273 the rMSE was used:

$$rMSE(\hat{\mathbf{X}}) = \frac{1}{Q} \sum_{q=1}^Q \frac{\|\hat{\mathbf{x}}_q - \mathbf{x}_q\|_F^2}{\|\mathbf{x}_q\|_F^2}, \quad (19)$$

274 where  $\mathbf{x}_q$  represents the  $q$ -th CNNMSI from our dataset with  $Q$  MSIs and  $\hat{\mathbf{x}}_q$  its corresponding  
275 reconstruction computed by (3).

276 6.2.2. Cohen's Kappa Coefficient

277 Cohen's kappa coefficient is a very robust metric used to measure reliability of multi-class and  
278 imbalanced class classification algorithms. It is computed by

$$\kappa = \frac{\rho_o - \rho_e}{1 - \rho_e} \quad (20)$$

279 where  $\rho_o$  is the observed agreement, and  $\rho_e$  is the expected agreement. This metric will always produce  
280 values less than or equal to 1, where 1 means perfect agreement. Negative values indicate no agreement.  
281 i.e., futile classification.

282 6.2.3. Pixel Accuracy (PA)

283 We used the PA metric to compute a ratio between the amount of correctly classified pixels and  
284 the total number of pixels as follows. Given a confusion matrix relating the True Positive (TP), True  
285 Negatives (TN), False Positives (FP) and False Negatives (FN), the PA is computed by

$$PA = \frac{\sum_{c=1}^C \tau_{cc}}{\sum_{c=1}^C \sum_{d=1}^C \tau_{cd}} = \frac{TP + TN}{TP + TN + FP + FN} \quad (21)$$

286 where  $c$  is the number of class for  $c = 1, \dots, C$  and  $\tau_{cc}$  is the amount of pixels of class  $c$  correctly  
287 assigned to class  $c$  i.e., TP and TN, and  $\tau_{cd}$  is the amount of pixels of class  $c$  inferred to belong to class  
288  $d$ . Despite this metric is wide used, it is not a totally fair metric for imbalanced classes. In this work we  
289 used this metric with comparison purposes. However, we also used metrics more in line with multi  
290 class classification tasks.

291 6.2.4. Precision

292 Another metric used in this work as a performance evaluation metric in multiclass classification  
293 is precision. This is a metric that measures the percentage of pixels from class  $c$  correctly classified. It  
294 is computed with the following equation

$$\Psi_c = \frac{\tau_{cc}}{\sum_{d=1}^C \tau_{cd}} = \frac{TP}{TP + FP} \quad (22)$$

295 where  $\Psi_c$  denotes the precision of class  $c$ , which is the number of TP divided by the TP plus FP.

<sup>296</sup> 6.2.5. Recall or Sensitivity

<sup>297</sup> Recall, or also known as sensitivity is a metric that indicates the proportion of pixels classified as  
<sup>298</sup> class  $c$  that actually belong to class  $c$ . It is computed with the following equation

$$v_c = \frac{\tau_{cc}}{\sum_{d=1}^C \tau_{dc}} = \frac{TP}{TP + FN} \quad (23)$$

<sup>299</sup> where  $v_c$  denotes the recall of class  $c$  for  $c = 1, \dots, C$ .

<sup>300</sup> 6.2.6. F1 Score

<sup>301</sup> In order to summarize precision and recall in one only metric, we use the F1 score, which is  
<sup>302</sup> computed by

$$F1 = \frac{2\Psi v}{\Psi + Y} \quad (24)$$

<sup>303</sup> This metric provides a very appropriate measure of multiclass classification for imbalanced dataset.

<sup>304</sup> 7. Discussion and Comparison

<sup>305</sup> 8. Conclusions

<sup>306</sup> 8.1. Figures, Tables and Schemes

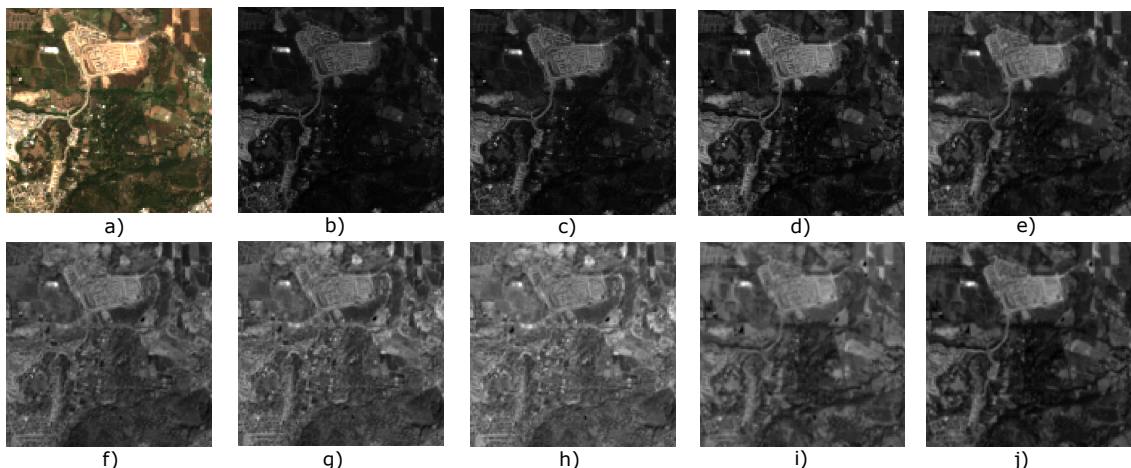


**Figure 6.** Original Sentinel-2 spectral bands, a) True color image, b) to j) 1st to 9th spectral band respectively.

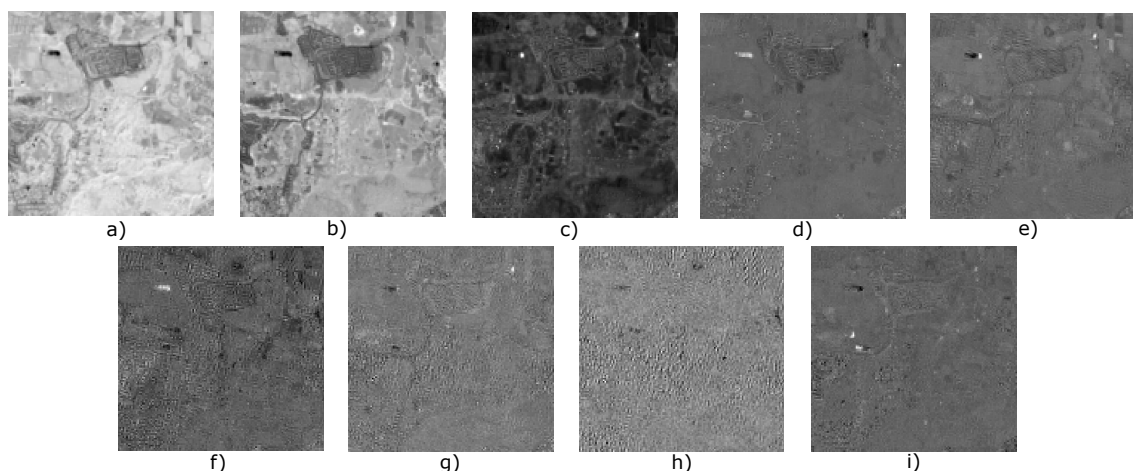


**Figure 7.** Tensor bands from the Tucker Decomposition, a) to i) 1st to 9th band respectively.

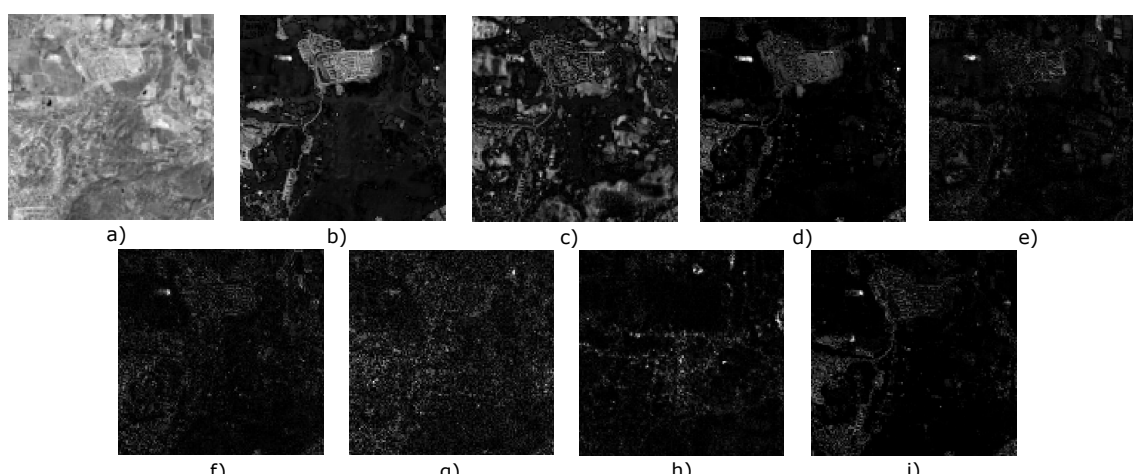


**Figure 8.** Tensor bands from the Non-negative Tucker Decomposition, a) to i) 1st to 9th band respectively.

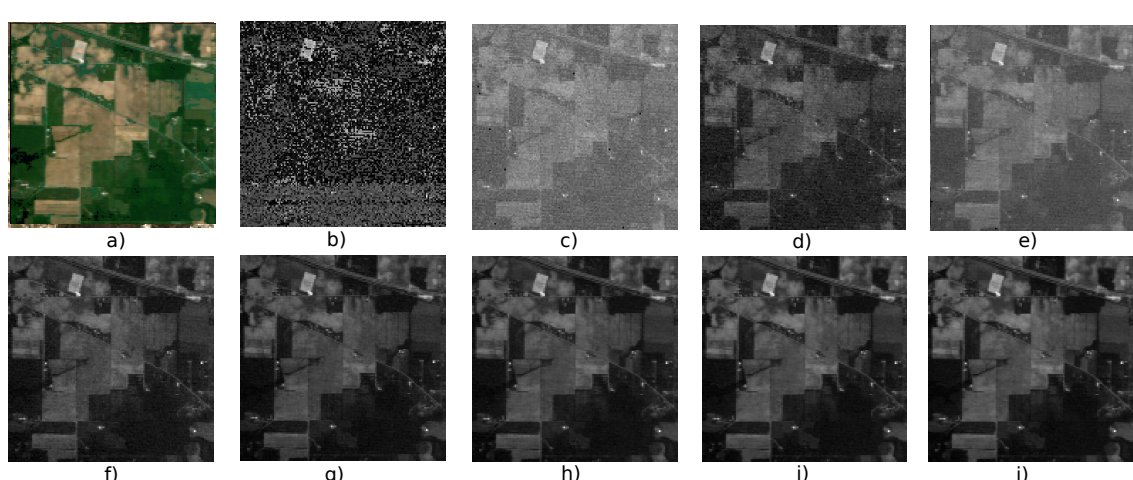


**Figure 9.** Original Sentinel-2 spectral bands.

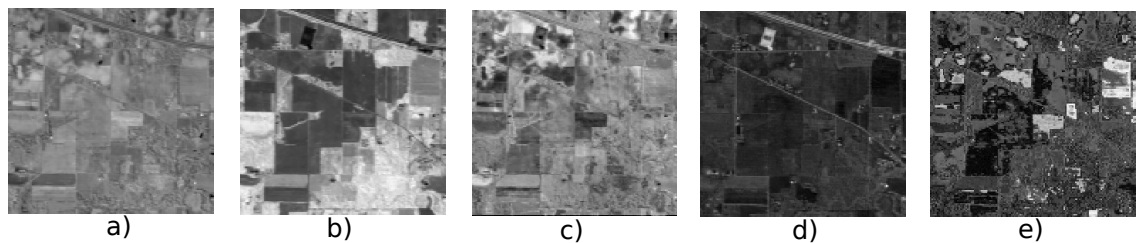


**Figure 10.** Tucker Decomposition Tensor bands.

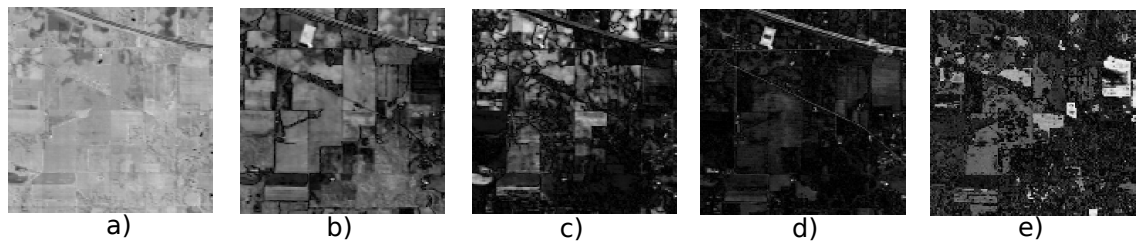


**Figure 11.** Nonnegative Tucker Decomposition Tensor bands.

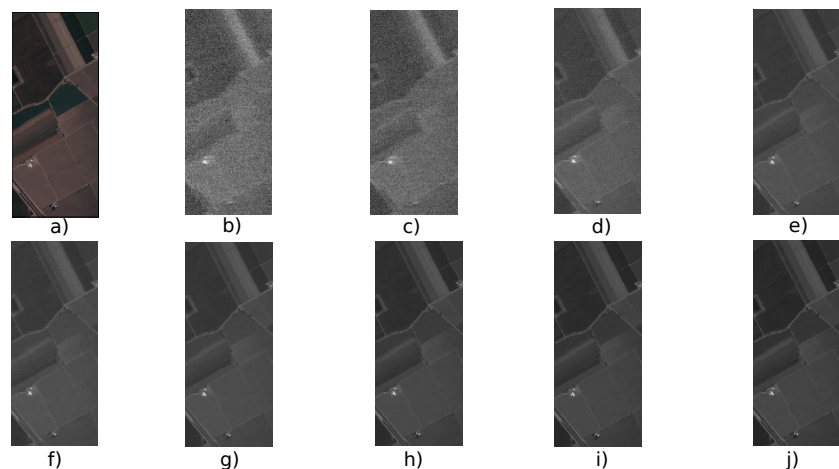


**Figure 12.** Original Sentinel-2 spectral bands.

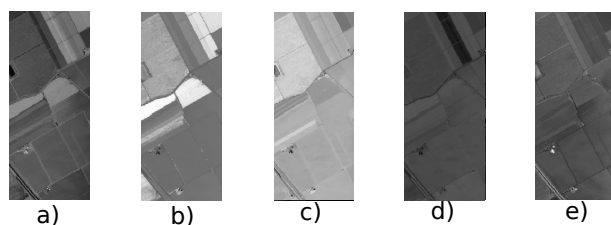


**Figure 13.** Tucker Decomposition Tensor bands.

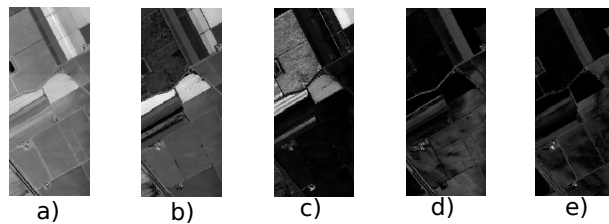


**Figure 14.** Nonnegative Tucker Decomposition Tensor bands.

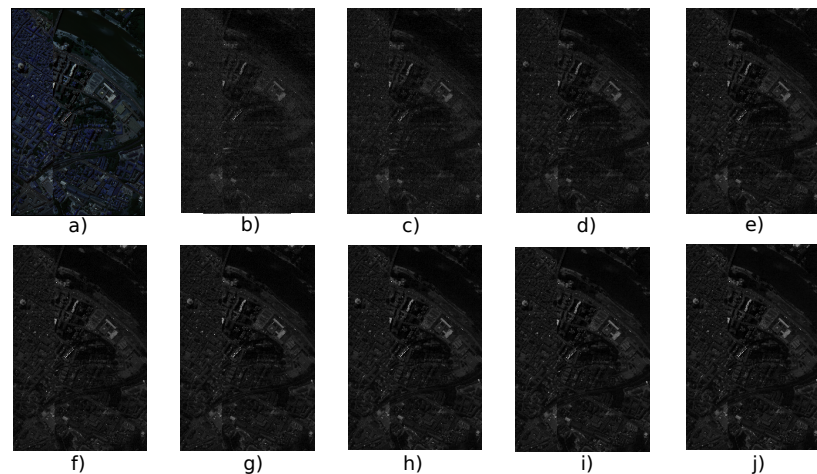


**Figure 15.** Original Sentinel-2 spectral bands.

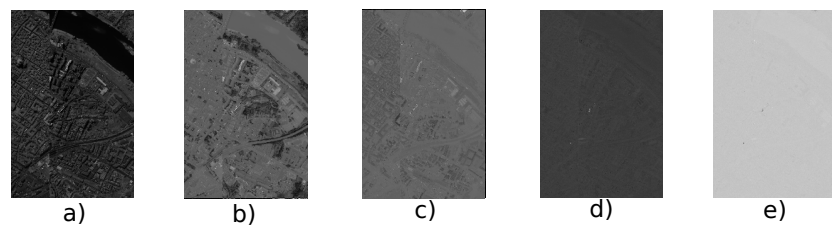


**Figure 16.** Tucker Decomposition Tensor bands.

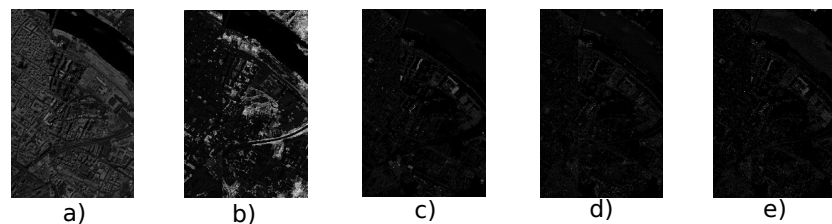
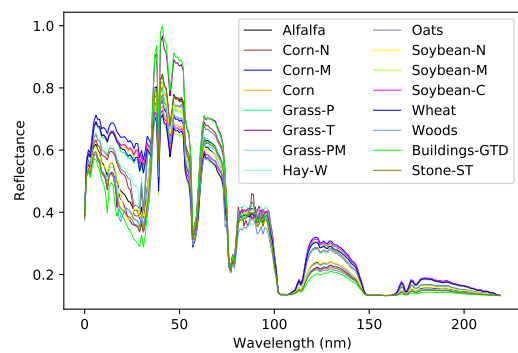
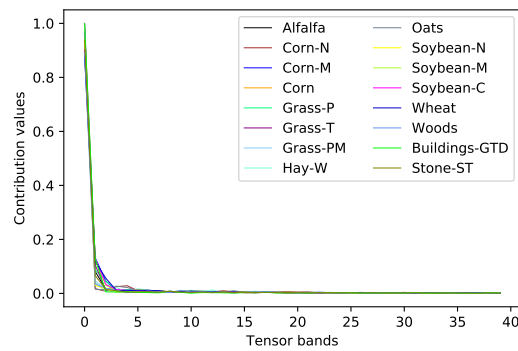


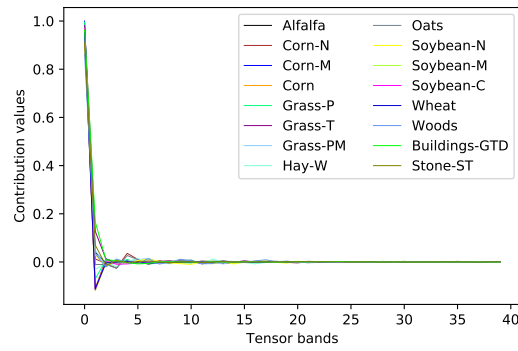
**Figure 17.** Nonnegative Tucker Decomposition Tensor bands.



(a)

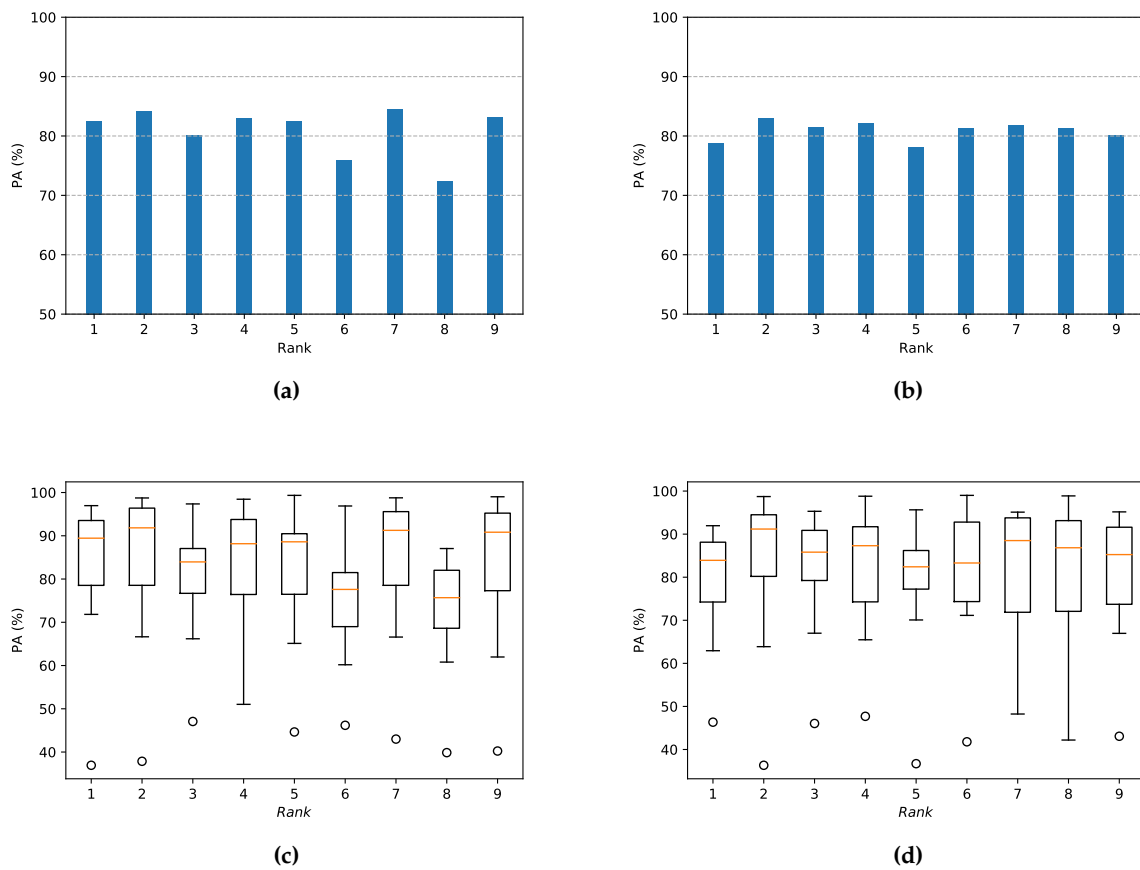


(b)

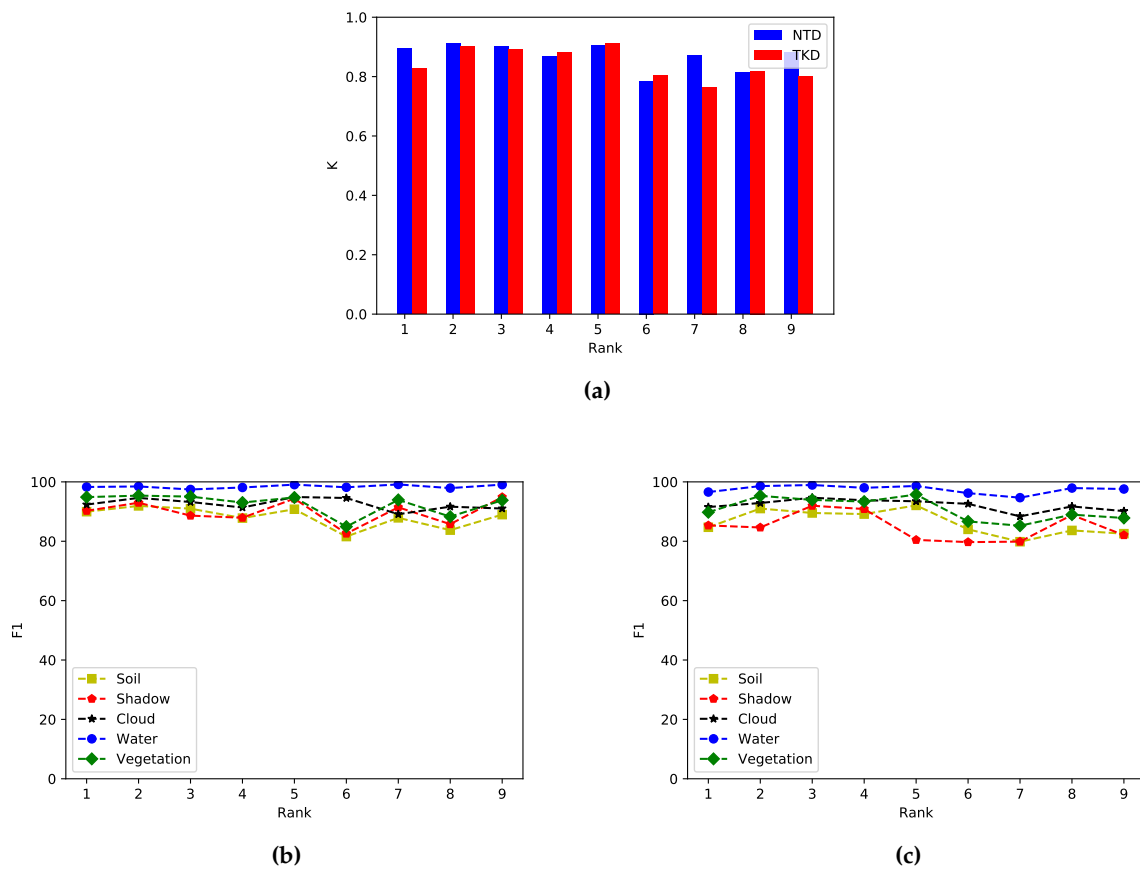


(c)

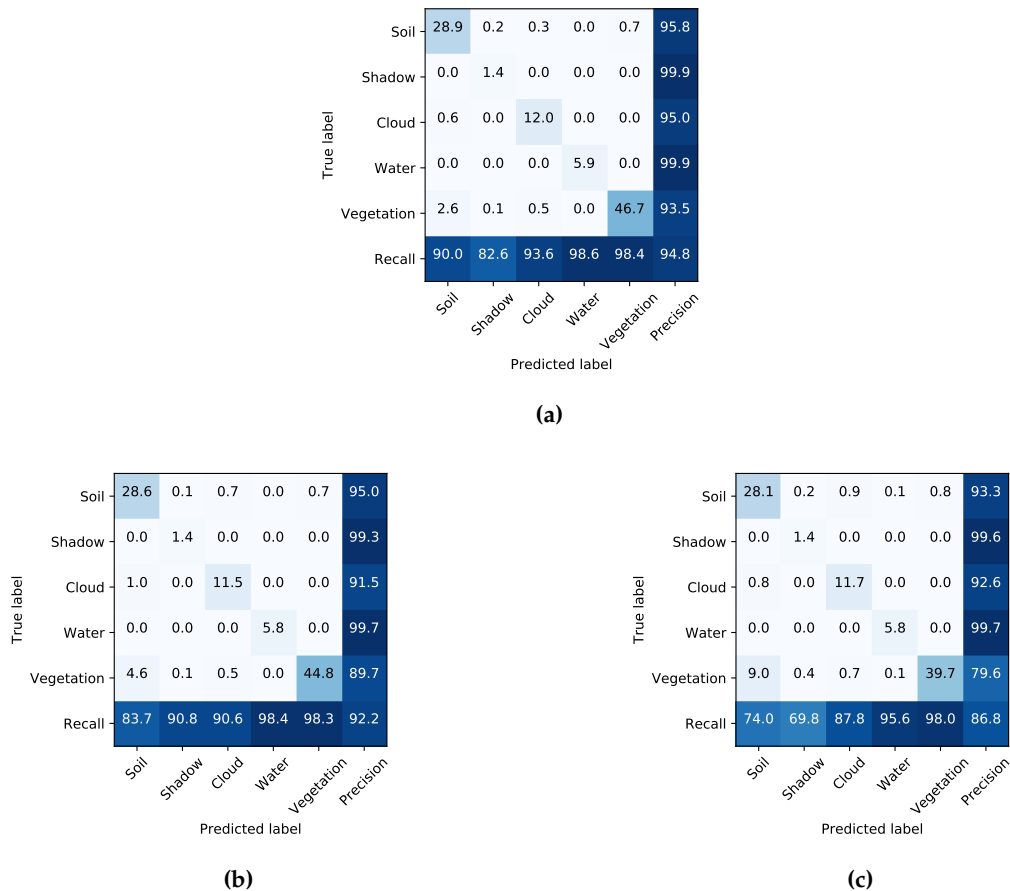
**Figure 18.** Indian Pines Spectral Signatures a) Original, b) NTD and c) TKD



**Figure 19.** Pixel accuracy vs Rank results a) Comparative bar plot NTKD and TKD, b) Comparative bar plot NTKD and TKD c) Box and whiskers plot for NTKD, and d) Box and whiskers plot for TKD



**Figure 20.** Performance evaluation metrics. a) Kappa score comparison NTD vs TKD, b) F1 for NTD and c) F1 for TKD

**Figure 21.** Confusion matrix for a) Sentinel-2 original dataset, b) NTD, c) TKD.

**307 Author Contributions:** Conceptualization, J.L.; formal analysis, D.T.; investigation, J.L.; methodology, J.L., D.T.,  
**308** and C.A.; resources, C.A.; software, J.L.; supervision, D.T. and C.A.; validation, D.T. and C.A.; writing—original  
**309** draft, J.L. and D.T.

**310 Funding:** This work was supported by the National Council of Science and Technology CONACYT of Mexico  
**311** under grant XXXXXXXX.

**312 Acknowledgments:**

**313 Conflicts of Interest:** The authors declare no conflict of interest.

**314 Abbreviations**

**315** The following abbreviations are used in this manuscript:

ANN	Artificial Neural Network
CNN	Convolutional neural network
CPD	Canonical Polyadic Decomposition
DL	Deep Learning
FCN	Fully Convolutional Network
HOOI	Higher-Order Orthogonal Iteration
HOSVD	Higher-Order Singular Value Decomposition

**318 References**

- Tempfli, K.; Huurneman, G.; Bakker, W.; Janssen, L.; Feringa, W.; Gieske, A.; Grabmaier, K.; Hecker, C.; Horn, J.; Kerle, N.; et al. *Principles of Remote Sensing: An Introductory Textbook*, 4th ed.; ITC: Geneva, Switzerland, 2009.

- 322 2. He, Z.; Hu, J.; Wang, Y. Low-rank tensor learning for classification of hyperspectral image with limited  
323 labeled sample. *IEEE Signal Process.* **2017**, *145*, 12–25.
- 324 3. Richards, A.; Xiuping, J.J. Band selection in sentinel-2 satellite for agriculture applications. In *Remote Sensing*  
325 *Digital Image Analysis*, 4th ed.; Springer-Verlag: Berlin, Germany, 2006.
- 326 4. Zhang, T.; Su, J.; Liu, C.; Chen, W.; Liu, H.; Liu, G. Band selection in sentinel-2 satellite for agriculture  
327 applications. In Proceedings of the 23rd International Conference on Automation & Computing, University  
328 of Huddersfield, Huddersfield, UK, 7–8 September 2017.
- 329 5. Xie, Y.; Zhao, X.; Li, L.; Wang, H. Calculating NDVI for Landsat7-ETM data after atmospheric correction  
330 using 6S model: A case study in Zhangye city, China. In Proceedings of the 18th International Conference on  
331 Geoinformatics, Beijing, China, 18–20 June 2010.
- 332 6. Gao, B. NDWI—A normalized difference water index for remote sensing of vegetation liquid water from  
333 space. *Remote Sens. Environ.* **1996**, *58*, 1–6.
- 334 7. Ham, J.; Chen, Y.; Crawford, M.; Ghosh, J. Investigation of the random forest framework for classification of  
335 hyperspectral data. *IEEE Trans. Geosci. Remote Sens.* **2005**, *43*, 492–501.
- 336 8. Hearst, Marti A. Support Vector Machines. *IEEE Intell. Syst.* **1998**, *13*, 18–28.
- 337 9. Huang, X.; Zhang, L. An SVM Ensemble Approach Combining Spectral, Structural, and Semantic Features  
338 for the Classification of High-Resolution Remotely Sensed Imagery. *IEEE Trans. Geosci. Remote Sens.*  
339 **2013**, *51*, 257–272.
- 340 10. Delalieux, S.; Somers, B.; Haest, B.; Spanhove, T.; Vanden Borre, J.; Mucher, S. Heathland conservation  
341 status mapping through integration of hyperspectral mixture analysis and decision tree classifiers.  
*Remote Sens. Environ.* **2012**, *126*, 222–231.
- 343 11. Kemker, R.; Salvaggio, C.; Kanan, C. Algorithms for semantic segmentation of multispectral remote sensing  
344 imagery using deep learning. *ISPRS J. Photogramm. Remote Sens.* **2018**, *145*, 60–77.
- 345 12. Pirotti, F.; Sunar, F.; Piragnolo, M. Benchmark of machine learning methods for classification of a sentinel-2  
346 image. In Proceedings of the XXIII ISPRS Congress, Prague, Czech Republic, 12–19 July 2016.
- 347 13. Mateo-García, G.; Gómez-Chova, L.; Camps-Valls, G. Convolutional neural networks for multispectral image  
348 cloud masking. In Proceedings of the IGARSS, Fort Worth, TX, USA, 23–28 July 2017.
- 349 14. Guo, X.; Huang, X.; Zhang, L.; Zhang, L.; Plaza, A.; Benediktsson, J. A. Support Tensor Machines for  
350 Classification of Hyperspectral Remote Sensing Imagery. *IEEE Trans. Geosci. Remote Sens.* **2016**, *54*, 3248–3264.
- 351 15. Cichocki, A.; Mandic, D.; De Lathauwer, L.; Zhou, G.; Zhao, Q.; Caiafa, C.; Phan, H. Tensor Decompositions  
352 for Signal Processing Applications: From two-way to multiway component analysis. *IEEE Signal Process. Mag.*  
353 **2015**, *32*, 145–163.
- 354 16. Jolliffe, I.T. *Principal Component Analysis*, 2nd ed.; Springer Verlag: New York, NY, USA, 2002.
- 355 17. Kolda, T.; Bader, B. Tensor Decompositions and Applications. *SIAM Rev.* **2009**, *51*, 455–500.
- 356 18. Lopez, J.; Santos, S.; Torres, D.; Atzberger, C. Convolutional Neural Networks for Semantic Segmentation  
357 of Multispectral Remote Sensing Images. In Proceedings of the LATINCOM, Guadalajara, Mexico,  
358 14–16 November 2018.
- 359 19. European Space Agency. Available online: <https://sentinel.esa.int/web/sentinel/missions/sentinel-2>  
360 (accessed on 15 July 2019).
- 361 20. Kemker, R.; Kanan, C. Deep Neural Networks for Semantic Segmentation of Multispectral Remote Sensing  
362 Imagery. *arXiv* **2017**, arXiv:abs/1703.06452.
- 363 21. Hamida, A.; Benoît, A.; Lambert, P.; Klein, L.; Amar, C.; Audebert, N.; Lefèvre, S. Deep learning for  
364 semantic segmentation of remote sensing images with rich spectral content. In Proceedings of the IGARSS,  
365 Fort Worth, TX, USA, 23–28 July 2017.
- 366 22. Wang, Q.; Lin, J.; Yuan, Y. Salient Band Selection for Hyperspectral Image Classification via Manifold  
367 Ranking. *IEEE Trans. Neural Netw. Learn. Syst.* **2016**, *27*, 1279–1289.
- 368 23. Li, S.; Qiu, J.; Yang, X.; Liu, H.; Wan, D.; Zhu, Y. A novel approach to hyperspectral band selection based on  
369 spectral shape similarity analysis and fast branch and bound search. *Eng. Appl. Artif. Intell.* **2014**, *27*, 241–250.
- 370 24. Zhang, L.; Zhang, L.; Tao, D.; Huang, X.; Du, B. Compression of hyperspectral remote sensing images by  
371 tensor approach. *Neurocomputing* **2015**, *147*, 358–363.
- 372 25. Astrid, M.; Lee, Seung-Ik. CP-decomposition with Tensor Power Method for Convolutional Neural Networks  
373 compression. In Proceedings of the BigComp, Jeju, Korea, 13–16 February 2017.
- 374 26. Chien, J.; Bao, Y. Tensor-factorized neural networks. *IEEE Trans. Neural Networks Learn. Syst.* **2018**, *29*, 1998–2011.

- 375 27. An, J.; Lei, J.; Song, Y.; Zhang, X.; Guo J. Tensor Based Multiscale Low Rank Decomposition for Hyperspectral  
376 Images Dimensionality Reductio. *Remote Sens.* **2019**, *11*, 1485.
- 377 28. Li, J.; Liu, Z. Multispectral Transforms Using Convolution Neural Networks for Remote Sensing Multispectral  
378 Image Compression. *Remote Sens.* **2019**, *11*, 759.
- 379 29. An, J.; Song, Y.; Guo, Y.; Ma, X.; Zhang, X. Tensor Discriminant Analysis via Compact Feature Representation  
380 for Hyperspectral Images Dimensionality Reduction. *Remote Sens.* **2019**, *11*, 1822.
- 381 30. Absil, P.-A.; Mahony, R.; Sepulchre, R. *Optimization Algorithms on Matrix Manifolds*, 1st ed.; Princeton  
382 University Press: Princeton, NJ, USA, 2007.
- 383 31. De Lathauwer, L.; De Moor, B.; Vandewalle, J. On the best rank-1 and rank-( $R_1, R_2, \dots, R_N$ ) approximation  
384 of higher-order tensors. *SIAM J. Matrix Anal. Appl.* **2000**, *21*, 1324–1342.
- 385 32. Goodfellow, I.; Bengio, Y.; Courville, A. *Deep Learning*, 1st ed.; MIT Press, 2016.
- 386 33. Sheehan, B. N.; Saad, Y. Higher Order Orthogonal Iteration of Tensors (HOOI) and its Relation to PCA and  
387 GLRAM. In Proceedings of the 7th SIAM International Conference on Data Mining, Minneapolis, MN, USA,  
388 26–28 April 2007.
- 389 34. Badrinarayanan, V.; Kendall, A.; Cipolla, R. SegNet: A Deep Convolutional Encoder-Decoder Architecture  
390 for Image Segmentation. *IEEE Trans. Pattern Anal. Mach. Intell.* **2017**, *39*, 2481–2495.
- 391 35. De Lathauwer, L.; De Moor, B.; Vandewalle, J. A Multilinear Singular Value Decomposition. *SIAM J. Matrix  
392 Anal. Appl.* **2000**, *21*, 1253–1278.
- 393 36. Rodes, I.; Inglada, J.; Hagolle, O.; Dejoux, J.; Dedieu, G. Sampling strategies for unsupervised classification  
394 of multitemporal high resolution optical images over very large areas. In Proceedings of the 2012 IEEE  
395 International Geoscience and Remote Sensing Symposium, Munich, Germany, 22–27 July 2012.

396 **Sample Availability:** Samples of the compounds ..... are available from the authors.

397 © 2020 by the authors. Submitted to *Remote Sens.* for possible open access publication  
398 under the terms and conditions of the Creative Commons Attribution (CC BY) license  
399 (<http://creativecommons.org/licenses/by/4.0/>).